$NaHCO_3$ addition enhances water permeance and Ca/haloacetic acids selectivity of nanofiltration membranes for drinking water treatment

Li Long,[1] Lu Elfa Peng,[1] Shenghua Zhou,[1] Qimao Gan,[1] Xianhui Li,[2] Jingyi Jiang,[3] Jiarui Han,[3] Xiangru Zhang,[3] Hao Guo,[1,4]* and Chuyang Y. Tang[1]*

[1] Membrane-based Environmental & Sustainable Technology Group, Department of Civil Engineering, The University of Hong Kong, Pokfulam, Hong Kong SAR, China.

[2] Key Laboratory for City Cluster Environmental Safety and Green Development of the Ministry of Education, School of Ecology, Environment and Resources, Guangdong University of Technology, Guangzhou, 510006, China.

[3] Department of Civil and Environmental Engineering, The Hong Kong University of Science & Technology, Clean Water Bay, Kowloon, Hong Kong SAR, China.

[4] Institute of Environment and Ecology, Tsinghua Shenzhen International Graduate School, Tsinghua University, Shenzhen 518055, China.

* Corresponding authors:

Dr. Hao Guo, phone: +86-15889350923, e-mail address: guohao@sz.tsinghua.edu.cn

Prof. Chuyang Y. Tang, phone: +852-28591976, e-mail address: tangc@hku.hk

Abstract

The existence of disinfection by-products such as haloacetic acids (HAAs) in drinking water severely threatens water safety and public health. Nanofiltration (NF) is a promising strategy to remove HAAs for clean water production. However, NF often possesses overhigh rejection of essential minerals such as calcium. Herein, we developed highly selective NF membranes with tailored surface charge and pore size for efficient rejection of HAAs and high passage of minerals. The NF membranes were fabricated through interfacial polymerization (IP) with $NaHCO_3$ as an additive. The $NaHCO_3$-tailored NF membranes exhibited high water permeance up to ~24.0 L m^{-2} h^{-1} bar^{-1} (more than doubled compared with the control membrane) thanks to the formation of stripe-like features and enlarged pore size. Meanwhile, the tailored membranes showed enhanced negative charge, which benefitted their rejection of HAAs and passage of Ca and Mg. The higher rejection of HAAs (e.g., > 90%) with the lower rejection of minerals (e.g., < 30% for Ca) allowed the NF membranes to achieve higher minerals/HAAs selectivity, which was significantly higher than those of commercially available NF membranes. The simultaneously enhanced membrane performance and higher minerals/HAAs selectivity would greatly boost water production efficiency and water quality. Our findings provide a novel insight to tailor the minerals/micropollutants selectivity of NF membranes for highly selective separation in membrane-based water treatment.

Keywords: haloacetic acids (HAAs); minerals/HAAs selectivity; drinking water treatment; carbonate chemistry; interfacial polymerization; polyamide nanofiltration membrane.

1. Introduction

Clean and sustainable drinking water is of the highest priority for public health in modern society (Tao and Xin, 2014; Villanueva et al., 2023). Disinfection is a widely adopted strategy to inactivate bacteria and pathogens in water, ensuring a safe drinking water supply (Jütte et al., 2023). However, it often comes with critical concerns about the formation of toxic and harmful disinfection by-products (DBPs) (Helte et al., 2022). For example, haloacetic acids (HAAs), a most abundant group of halogenated DBPs, can be generated during the disinfection process through the reaction between natural organic matter and disinfectants (e.g., chlorine) (Lee et al., 2022; Liu et al., 2022b). Long-term exposure to HAAs might increase the risk of bladder cancer (Costet et al., 2011; Li and Mitch, 2018; Liu et al., 2022a). Five of HAAs are regulated by the US EPA in the disinfectants/disinfection byproducts (D/DBP) rule (Mazhar et al., 2020). Therefore, it is imperative to control or remove HAAs in drinking water.

To date, various technologies such as adsorption (Jiang et al., 2018; Samonte et al., 2022) and catalysis (Cai et al., 2021; Li et al., 2022) have been reported to remove HAAs from water. Activated carbon is a commonly used adsorbent with a typical removal efficiency of ~80% for HAAs (Jiang et al., 2018). In addition, biochar (Long et al., 2017), polymer resin (Yin et al., 2020), and graphene oxide (Liu et al., 2022c) have also been reported as potential candidates for the adsorption of HAAs. However, these adsorbents usually require additional regeneration steps after the saturation of their capacity, which would compromise the overall process efficiency for sustainable water supply. Recently, photocatalysis has been investigated to degrade HAAs using the highly reactive free radicals (e.g., ·OH and $SO_4^{\cdot-}$) generated during the process (Wang et al., 2017; Zhang et al., 2022). For example, Wang et al. reported that ultraviolet photolysis could degrade HAAs with a removal efficiency of over 90%

(Wang et al., 2017). Despite the high removal of HAAs, photocatalysis often needs advanced photocatalysts and sufficient light conditions, which significantly increase its cost and aggravate the operational burden.

Nanofiltration (NF) is a promising alternative for HAAs removal in drinking water treatment (Guo et al., 2022b; Tang et al., 2018). Even if precursors could be removed from raw water to reduce HAA formation (Ding et al., 2019), additional HAAs may form in the distribution systems (Ding et al., 2019; Yan et al., 2022). For example, organic matter released from biofilms may react with residual disinfectants (e.g., chlorine), and the resulting HAAs necessitate their efficient removal for point-of-use treatment. Existing commercial NF membranes (e.g., NF90) could achieve relatively high rejection for HAAs (Yang et al., 2017a; Yang et al., 2017b) by their selective rejection polyamide layers. However, they often show overhigh rejection of minerals (e.g., > 99.0% of Ca^{2+} and > 99.5% of Mg^{2+} by the NF90 membrane) (Yang et al., 2017b), which would lead to insufficient minerals in the product water thereby challenging the water quality and public health. In general, the rejection of HAAs and minerals by NF membranes is mainly governed by the effective pore size and surface charge of its polyamide layer (Castaño Osorio et al., 2022; Guo et al., 2022a). Small pore size can lead to strong size exclusion and thus enhance membrane rejection of both HAAs and minerals (Yang et al., 2017b). Moreover, small pore size would sacrifice membrane water permeance due to the high water transport resistance across the membrane (He et al., 2022). On the other hand, the bigger pore size might lead to reduced rejection of HAAs due to the weakened size exclusion. In contrast, a negative surface charge would simultaneously improve the rejection of negatively charged HAAs (Yang et al., 2017b) and the passage of positively charged minerals through enhanced electrostatic interactions (Dai et al., 2020; Yuan et al., 2019). Therefore,

effective regulation of membrane pore size and surface charge is critical to tailor the selectivity of minerals/HAAs for high-quality drinking water production.

In principle, the properties of polyamide membranes can be regulated by controlling their formation conditions during the interfacial polymerization (IP) reaction (Li et al., 2021; Shao et al., 2022). A recent study reported the critical importance of aqueous carbonate chemistry on IP reaction for tailoring the surface morphology of polyamide reverse osmosis (RO) membranes (Peng et al., 2019). Bicarbonate ions in the aqueous amine solution could react with H^+ produced from the IP reaction to generate CO_2 (Ma et al., 2019; Peng et al., 2019). Under the influence of local heating during IP (Ukrainsky and Ramon, 2018), CO_2 degasses as nanobubbles (Ma et al., 2018; Song et al., 2020), whose encapsulation in RO polyamide layers could result in a foamed nanostructure to improve their separation performance.

Inspired by the above findings, we envision that the aqueous carbonate chemistry might play an important role during the formation of polyamide NF membranes thereby affecting their membrane properties and separation performance. In this work, we used sodium bicarbonate ($NaHCO_3$) as an additive in the aqueous amine phase. By taking advantage of its reaction with the IP by-product H^+, we managed to tailor the morphology and chemistry of the resulting NF membranes to simultaneously achieve high water permeance and high minerals/HAAs selectivity. The membrane structure-chemistry-performance relationship revealed in this study has important implications for the future development of highly selective NF membranes.

2. Materials and methods

2.1. Materials and chemicals

A polyethersulfone (PES) ultrafiltration membrane (UP150, MICRODYN-NADIR)

was used as the substrate for the IP reaction. Piperazine (PIP, 99%), 1,3,5-benzenetricarbonyl trichloride (TMC, 98%) and $NaHCO_3$ (≥99.7%) used for NF membranes fabrication were all purchased from Sigma-Aldrich. Five HAAs, including bromoacetic acid (MBAA, 97%), bromochloroacetic acid (BCAA, 97%), dibromoacetic acid (DBAA, 97%), trichloroacetic acid (TCAA, ≥99%) and tribromoacetic acid (TBAA, 99%), were obtained from Sigma-Aldrich. *Table S1* shows the chemical structures and properties (e.g., chemical formula) of the five HAAs used in this study. Generally, HAAs exist as anions under environmental pH values. Sodium chloride (NaCl, Dieckmann), sodium sulphate (Na_2SO_4, Dieckmann), magnesium sulphate ($MgSO_4$, Dieckmann), magnesium chloride ($MgCl_2$, Uni-Chem) and calcium chloride ($CaCl_2$, Dieckmann) were used for salt rejection tests of NF membranes. Glycol (Dieckmann), glucose (Dieckmann), raffinose (Sigma-Aldrich) and dextran (D-chem) were used as neutral molecular probes to determine the effective pore size of the membranes. Six commercial NF membranes were used for comparison and benchmarking purposes. NF90 and NF270 were obtained from Dow Chemical Co. and four other NF membranes used for tap water purification (TWP-1 to TWP-4) were purchased from the local market.

2.2. NF membrane fabrication

NF membranes were fabricated through the following procedures (**Fig. 1**): (1) immersing a UP150 substrate into a 30 mL 1.0 wt.% PIP solution with a predetermined $NaHCO_3$ concentration (0, 0.01, 0.1, 0.5, or 1.0 M) for 2 min; (2) removing the residual PIP aqueous solution using a rubber roller; (3) soaking PIP-impregnated substrate in a 15 mL 0.1 wt.% TMC/hexane solution for 1 min; (4) rinsing the fabricated NF membranes with fresh hexane twice to remove unreacted TMC and heating these

membranes in an oven at 60 °C for 10 min. The fabricated membranes were denoted as NF-x, where x represents the molar concentration of $NaHCO_3$ in the PIP solution. All the membranes were stored in deionized water before further tests.

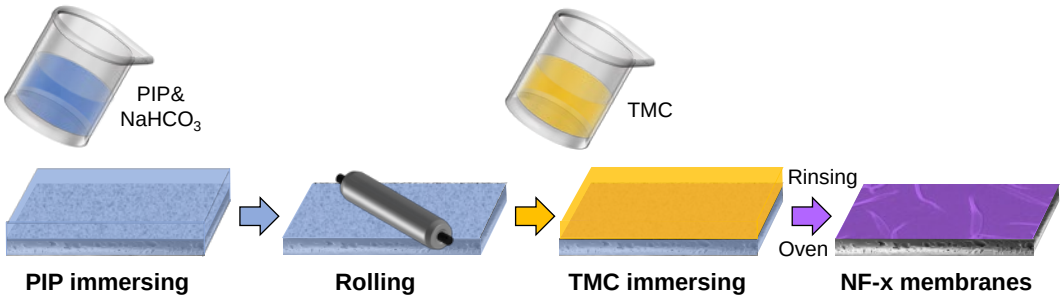

Fig. 1. Schematic diagram of NF-x membrane fabrication procedures.

2.3. Membrane characterization

A scanning electron microscope (SEM, S-4800, Hitachi) was used to characterize membrane morphology (Peng et al., 2020). Before the SEM characterization, membrane samples were dried and coated with a thin layer of gold using a sputter coater (SCD 005, BAL-TEC) (Gan et al., 2023). A Fourier transform infrared spectrometer equipped with an attenuated total refraction component (FTIR-ATR, iD5, Thermo Scientific) was used to determine the membrane surface functional groups (Gan et al., 2022). An X-ray photoelectron spectrometer (XPS, ULVAC X-tool) was applied to analyze the elemental composition on the membrane surface, which could be applied to calculate the crosslinking degree of polyamide layers (Wu et al., 2022). All membrane samples were thoroughly rinsed by deionized water and then dried in an oven at 40 °C overnight before the FTIR-ATR and XPS tests. A zeta potential analyzer (SurPASS 3, Anton Paar) was used to determine membrane surface charge with a pH ranging from 3 to 10 using a background electrolyte of 10 mM NaCl.

2.4. Filtration tests

Membrane filtration tests were performed using a laboratory cross-flow filtration system with two parallel cells at a room temperature of 25 ± 1 °C (Long et al., 2022). The membrane coupons were pre-compacted at 5 bar for 2 h, followed by the measurement of membrane separation performance at the same pressure. Membrane water permeance was determined by the following equations:

$$J_w = \frac{\Delta V}{\Delta t \times S} \quad (1)$$

$$A = \frac{J_w}{\Delta P - \Delta \pi} \quad (2)$$

where J_w (L m^{-2} h^{-1}) is the membrane water flux, Δt (h) is the sample collection time, S (m^2) is the effective filtration area (i.e., 2 cm^2), ΔV (L) is the volume of permeate sample, A (L m^{-2} h^{-1} bar^{-1}) is the membrane water permeance, ΔP (bar) is the applied hydraulic pressure, and $\Delta \pi$ (bar) is the osmotic pressure difference across the membrane.

Membrane rejection of salts was determined using 1000 ppm NaCl, Na_2SO_4, $MgSO_4$, $MgCl_2$, or $CaCl_2$ as a feed solution. Salt concentration values in permeate and feed samples were measured using a conductivity meter (Ultrameter II, Myron L). Membrane effective pore size was determined by performing the rejection tests of various neutral molecular probes (i.e., glycol, glucose, raffinose, or dextran) with a feed concentration of 200 ppm. The concentration of these probes was measured by a total organic carbon analyzer (TOC-L CPH, Shimadzu). The rejection tests of HAAs were conducted using a cocktail feed solution containing five HAAs (MBAA, BCAA, DBAA, TCAA, and TBAA) with a concentration of 200 ppb for each at pH 8. The concentration values of HAAs were determined by gas chromatography with an electron capture detector (GC-ECD, Agilent 7890A) according to previous literature (Jiang et al., 2017).

Both feed and permeate samples were collected after the 2-h pre-compaction to determine the membrane rejection. The solute rejection and permeability coefficient were calculated using the following equations:

$$R = \frac{C_f - C_p}{C_f} \quad (3)$$

$$B = \frac{1-R}{R} J_w \quad (4)$$

where R represents the solute rejection, C_f and C_p are the solute concentration in the feed and permeate samples, respectively, and B is the solute permeability coefficient.

Membrane selectivity parameters were determined using the following equation (Yang et al., 2019; Yang et al., 2022b; Zhao et al., 2021):

$$S_{i/j} = \frac{B_i}{B_j} \quad (6)$$

where $S_{i/j}$ is the solute/solute selectivity between solute i and j. For example, $S_{Ca/HAAs}$ represents the selectivity of Ca over HAAs.

3. Results and discussion

3.1. Membrane characterizations

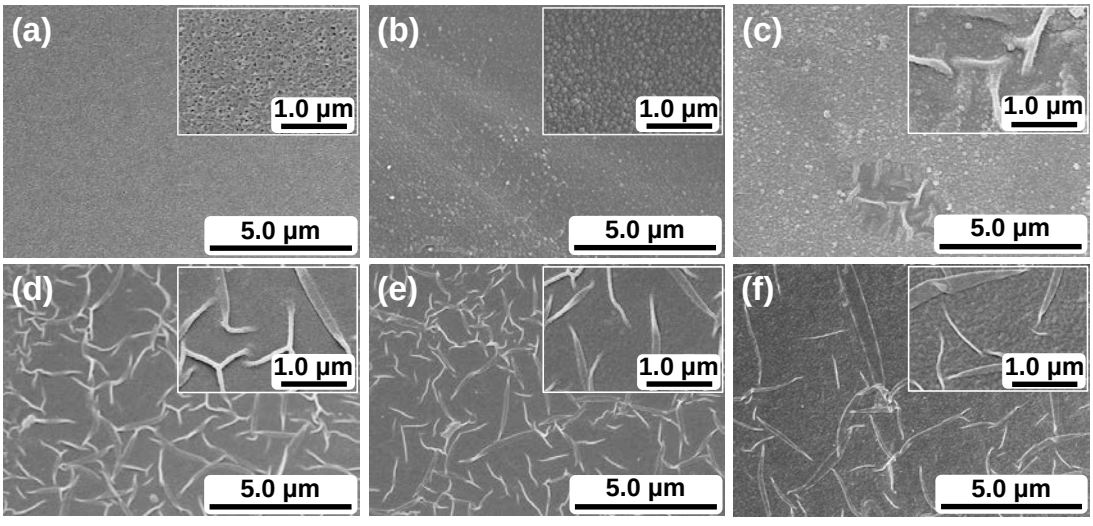

Fig. 2. SEM images of the **(a)** UP150 substrate, **(b)** NF-0, **(c)** NF-0.01, **(d)** NF-0.1, **(e)** NF-0.5, and **(f)** NF-1.0 membranes. The inserted images show the surface morphology

of various membranes at a high magnification.

Fig. 2 shows the surface morphology of the substrate and the prepared NF membranes. The substrate exhibits a porous surface with an average pore size of ~16 nm (**Fig. 2a** and *Fig. S1*). NF-0, the control membrane without $NaHCO_3$ addition, had a relatively smooth surface with a nodular-like structure (**Fig. 2b**). Its characteristic FTIR peak at ~1620 cm^{-1} (*Fig. S2*) suggests the successful fabrication of the polyamide rejection layer (Tang et al., 2009). The addition of $NaHCO_3$ resulted in the formation of stripe-like features on the membrane surfaces (**Fig. 2c-f**). NF membranes formed with higher $NaHCO_3$ concentration (i.e., NF-0.1 and NF-0.5) possessed enlarged size and enhanced coverage of stripes compared to that of the NF-0.01 membrane. Further increasing $NaHCO_3$ concentration to 1 M led to the increased width of stripes but with reduced coverage (**Fig. 2f**). According to the interfacial degassing theory (Ma et al., 2019; Peng et al., 2019), the IP reaction can generate H^+ to react with HCO_3^- and degas CO_2 from the aqueous phase during the exothermic formation of polyamide layer (Peng et al., 2022). These degassed CO_2 nanobubbles might be encapsulated in the polyamide layer thereby leading to the formation of the vaulted structure (Ma et al., 2019; Qiu et al., 2023), which might further collapse into stripe-like features (Jiang et al., 2020).

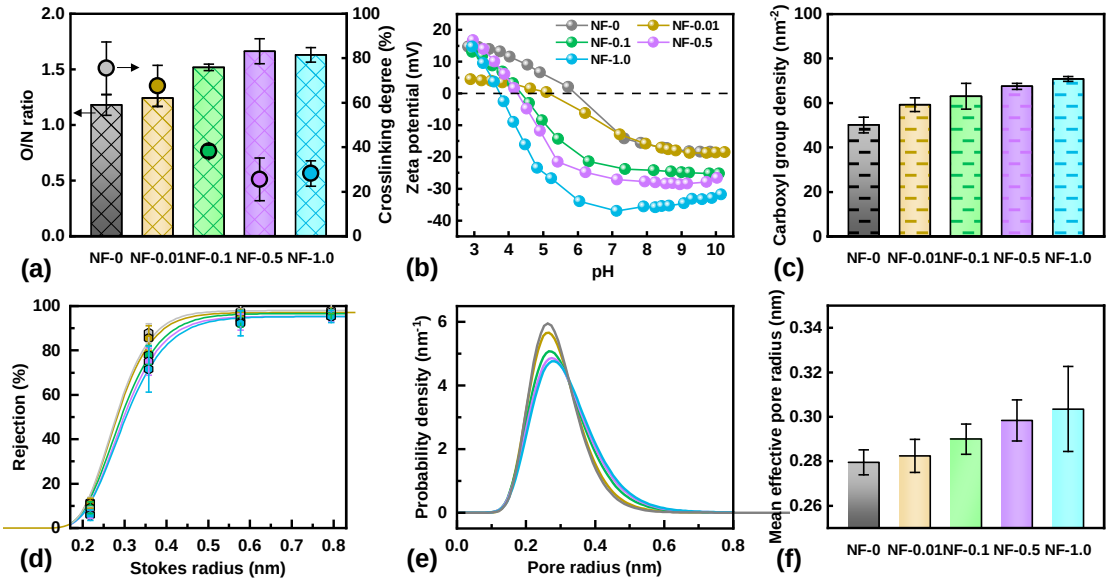

Fig. 3. (a) The O/N ratio and calculated crosslinking degree, **(b)** zeta potential analysis, **(c)** carboxyl group density of NF-x membranes (following the method of the references (Mo et al., 2012; Tiraferri and Elimelech, 2012)), (**d**) rejection of molecular probes as a function of Stokes radius of the molecules, **(e)** probability density function curves and estimated pore radius for the NF-x membranes, and (**f**) mean effective pore radius of NF-x membranes. The pore radius was estimated using the rejection data of neutral molecular probes from at least three independent experiments. The *p*-value between NF-0 and NF-0.5 membranes was 0.02, indicating a significant difference in the pore size of these two membranes. The detailed calculation procedures for crosslinking degree, carboxyl group density, and membrane pore radius can be found in *Supplementary Materials S3, S4* and *S5*, respectively.

The fabricated NF-x membranes showed increased O/N ratio at higher $NaHCO_3$ dosages, leading to the reduced crosslinking degree of their polyamide layers (**Fig. 3a**). One potential explanation is the competition between HCO_3^- and H^+ for OH^- in the alkaline PIP solution (e.g., pH of ~11.5 for 1% PIP solution), which weakens the ability of the solution for neutralizing H^+ – a byproduct from the IP reaction. Consistently, we observed that the surface zeta potential of the NF-x membranes became more negative at high $NaHCO_3$ concentrations (**Fig. 3b**). This can be attributed to a large number of carboxylic groups at a low crosslinking degree (Do et al., 2012). The analysis of carboxyl group density further indicated that the addition of $NaHCO_3$ resulted in more negatively charged NF-x membranes (**Fig. 3c**). In addition, the NF-x membranes

formed with a higher $NaHCO_3$ dosage demonstrated lower rejection of neutral molecular probes (**Fig. 3d**), whose rejection is mainly governed by size exclusion (Guo et al., 2017). Further pore size distribution analysis demonstrated that the membrane mean pore radius (r_p) increased from 0.279 nm for the NF-0 membrane to 0.304 nm for the NF-1.0 membrane (**Fig. 3e and f**).

3.2 Membrane separation performance

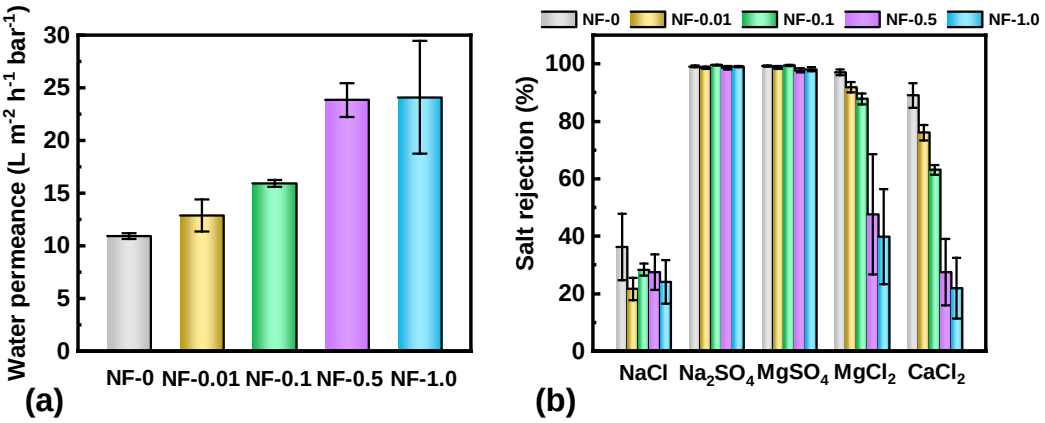

Fig. 4. Membrane separation performance: **(a)** pure water permeance and **(b)** rejection of various salts by the fabricated NF-x membranes. Test conditions: membrane separation performance was tested using a feed solution containing deionized water or a 1000 ppm salt solution (i.e., NaCl, Na_2SO_4, $MgSO_4$, $MgCl_2$, or $CaCl_2$). Pure water permeance and salt rejection were determined after a 2-h pre-compaction. The filtration tests were operated at 5 bar with a room temperature of ~ 25 ^oC.

The addition of $NaHCO_3$ resulted in the significantly enhanced pure water permeance up to ~24.0 L m^{-2} h^{-1} bar^{-1} for NF-0.5 and NF-1.0 membranes (**Fig. 4a**), which was more than doubled compared with NF-0 membrane (10.9 L m^{-2} h^{-1} bar^{-1}). This can be ascribed to their larger membrane pore size (**Fig. 3d**), which greatly reduced the water transport resistance across the membrane (Dai et al., 2022). In addition, the formed stripe-like features could also facilitate water transport by providing additional transport pathways through the voids underneath the stripes (Dai et al., 2023; Hu et al., 2023; Shao et al., 2022; Zhang et al., 2021). All the NF-x membranes maintained high

rejection of ~99% for Na_2SO_4 and $MgSO_4$ while their rejection of NaCl were generally lower than 40% (**Fig. 4b**). The high rejection of the sulphate salts could be attributed to (1) the larger size of SO_4^{2-} compared with Cl^- and (2) the strong electrostatic repulsion between the divalent SO_4^{2-} and negatively charged membrane surface (**Fig. 3b**) (Childress and Elimelech, 2000; Yang et al., 2022a). On the other hand, membrane rejection of $CaCl_2$ decreased from 89% for the NF-0 membrane to 22% for the NF-1.0 membrane. A similar trend was also observed for $MgCl_2$. The significantly reduced rejection of $CaCl_2$ and $MgCl_2$ could be explained by the combined effects of stronger Donnan effect for the divalent cations in addition to the weakened size exclusion for the NF-x membranes formed at high $NaHCO_3$ concentrations (Childress and Elimelech, 2000; Yuan et al., 2019). Such low rejection of Ca^{2+} and Mg^{2+} indicates greater mineral passage through the membranes, which could potentially address the critical deficit of conventional NF membranes with depleted essential minerals in product water.

3.3 HAAs rejection by NF-x membranes

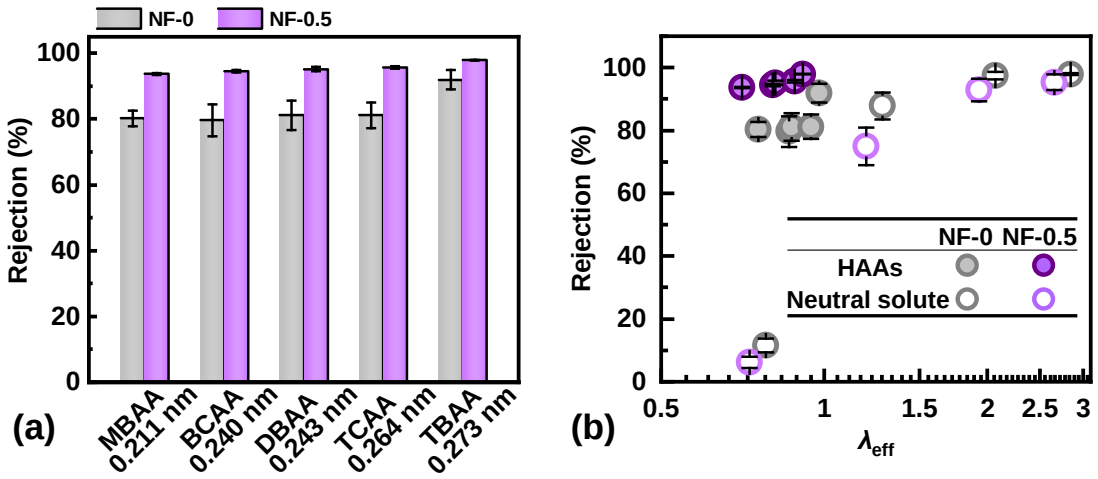

Fig. 5. (a) The rejection test of five HAAs by the NF-0 and NF-0.5 membranes. Stokes radius of the HAAs is provided in the figure. **(b)** The rejection of HAAs and neutral molecular probes as a function of λ_{eff}, which is the ratio of the solute Stokes radius over the membrane mean pore radius (Yang et al., 2017b). Test conditions: the rejection filtration was performed using a mixed solution containing 5 HAAs with a

concentration of 200 ppb for each. Both feed and permeate samples were collected for HAAs analysis after a 2-h pre-compaction. The HAAs rejection test was operated at 5 bar under the room temperature of ~ 25 ^{o}C.

As shown in **Fig. 5a**, both NF-0 and NF-0.5 membranes showed enhanced rejection of HAAs with larger Stokes radius (*Table S2*), which can be attributed to the stronger size exclusion (Yang et al., 2017a; Yang et al., 2017b). Moreover, the NF-0.5 membrane consistently exhibited higher rejection of 94-98% for HAAs than that of the NF-0 membrane (80-92%). To further elucidate the underlying rejection mechanisms, we analyzed the rejection of HAAs and neutral molecular probes as a function of normalized molecular size (λ_{eff}) (**Fig. 5b**), where λ_{eff} is the ratio of the solute Stokes radius over the membrane mean pore radius. Both NF-0 and NF-0.5 membranes showed relatively high rejection of molecular probes with $\lambda_{eff} > 1$ as a result of the strong size exclusion. In comparison, membrane rejection of the small neutral molecular probe ($\lambda_{eff} < 1$) was greatly reduced (< 15%) due to the significantly weakened size effect. In contrast, both membranes exhibited relatively high rejection of the negatively charged HAAs (≥ 80%) despite their small sizes ($\lambda_{eff} < 1$), which reveals the dominant role of electrostatic repulsion between the HAAs anions and the negatively charged membrane surface (Yang et al., 2017b).

It is also interesting to observe the different rejection performance of these two membranes. For each given neutral molecular probe, the NF-0.5 membrane showed lower rejection compared with the NF-0 control membrane (**Fig. 5b**), which can be readily explained by its larger pore size (**Fig. 3d**). On the contrary, for the negatively charged HAAs, the NF-0.5 membrane showed significantly higher rejection values compared with the control membrane despite the weakened size exclusion for NF-0.5 membrane. This counterintuitive result underpinned the critical role of enhanced electrostatic repulsion for the NF-0.5 membrane, which is consistent with its more

negatively charged surface charge (**Fig. 3b**).

3.4 Minerals/HAAs selectivity analysis

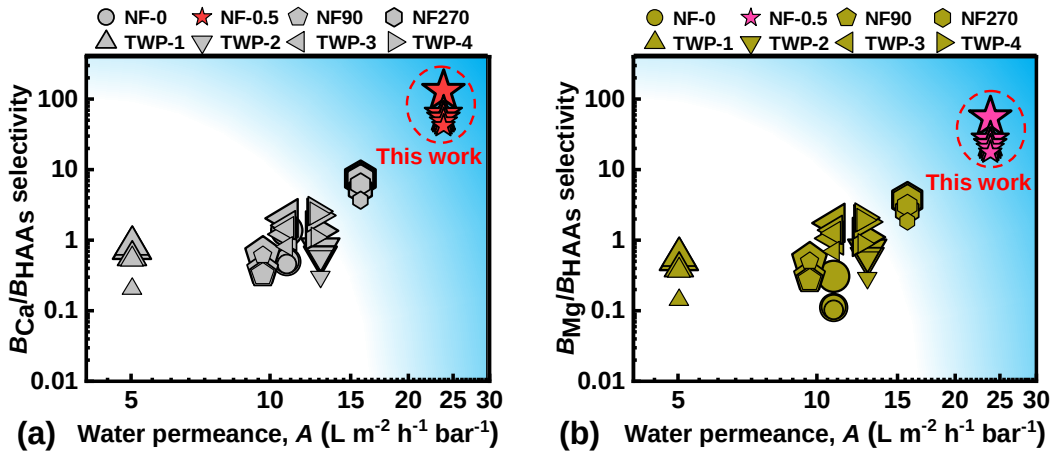

Fig. 6. Minerals/HAAs selectivity of NF membranes. **(a)** Ca/HAAs selectivity and **(b)** Mg/HAAs selectivity vs. water permeance for NF-0, NF-0.5, NF90, NF270, and four NF membranes used in tap water purifiers (TWP-1, TWP-2, TWP-3, and TWP-4). A is membrane pure water permeance, while B_{Ca}, B_{Mg}, and B_{HAAs} are the solute permeability coefficients of $CaCl_2$, $MgCl_2$, and HAAs, respectively. Symbols with larger sizes represent HAAs with greater molecular sizes (MBAA < BCAA < DBAA < TCAA < TBAA). NF90, NF270, and four TWP membranes are included as benchmarks. Their separation performance data were shown in *Table S2*.

Our results demonstrate that the control of membrane surface charge and pore size by simple $NaHCO_3$ addition could achieve simultaneously enhanced water permeance (**Fig. 4a**), passage of minerals (**Fig. 4b**), and rejection of HAAs (**Fig. 5a**). **Fig. 6** further benchmarks the minerals/HAAs selectivity and water permeance for the fabricated NF-x membranes (NF-0.5 and NF-0) against two commonly used commercial membranes (NF90 and NF270). Furthermore, four additional commercial NF membranes used in tap water purifiers (TWP-1, TWP-2, TWP-3, and TWP-4) were also included in the comparison. The NF-0.5 membrane exhibited the highest water permeance compared to other membranes. This high permeance is preferable for membrane-based water treatment due to potential benefits, such as reduced energy consumption (Yang et al., 2023). *Table S2* presents the membrane rejection data of mineral ions (Ca^{2+} and Mg^{2+})

and HAAs. All commercial NF membranes except NF270 showed relatively high rejections of mineral ions (> 90%) and HAAs (> 80%). Although the more permeable NF270 had lower rejections of Ca^{2+} (43.8%), its rejections of HAAs were also greatly reduced. As such, all the commercial NF membranes had relatively low Ca/HAAs selectivity (**Fig. 6a**). In contrast, the NF-0.5 membrane simultaneously possessed high rejection of HAAs (> 90%) and low rejection of Ca (< 30%). Correspondingly, its Ca/HAAs selectivity was an order of magnitude higher than those of the commercial NF membranes. Similar trend was also observed for the selectivity of Mg/HAAs, with NF-0.5 greatly outperforming the six commercial NF membranes (**Fig. 6b**). The high minerals/HAAs selectivity ensures sufficient passage of essential minerals together with the efficient removal of HAAs. The higher water permeance with better minerals/HAAs selectivity of NF-0.5 membrane simultaneously improves the quantity and quality of product water, which is desired for drinking water treatment.

4. Conclusions

In this study, we achieved the simultaneous tailoring of polyamide membrane surface charge and pore size using $NaHCO_3$ as an additive in the IP reaction. The addition of $NaHCO_3$ led to the formation of stripe-like features on the membrane surface as characterized by SEM. Further XPS and zeta potential analysis revealed that the $NaHCO_3$-doped membranes had less crosslinked polyamide layers with enhanced negative surface charge. Meanwhile, the tailored membranes showed enlarged pore radius (e.g., from 0.279 nm for the NF-0 membrane to 0.304 nm for the NF-1.0 membrane). The larger pore size together with the stripe-like morphology significantly improved membrane water permeance (e.g., over two times enhancement compared to the control membrane). On the other hand, the strong negative surface charge of the

$NaHCO_3$-doped membranes simultaneously improved their rejection of HAAs and passage of minerals thanks to the strengthened electrostatic interactions. The optimized membrane (NF-0.5) minerals/HAAs selectivity values were significantly higher than those of existing commercial NF membranes, including those used in tap water purifiers. These results suggest that the developed NF membranes could be a promising candidate for the highly selective removal of HAAs and maintenance of minerals in drinking water treatment. Our findings provide a new angle of simultaneous control of membrane physicochemical properties for highly selective solute/solute separation in membrane-based water treatment.

Declaration of Competing Interest

The authors declare that they have no known competing financial interests or personal relationships that could have appeared to influence the work reported in this paper.

Acknowledgment

This study was supported by a grant from the Research Grants Council of the Hong Kong Special Administration Region, China (GRF 17206122). We also thank the partial support from the Guangdong-Hong Kong Technology Cooperation Funding Scheme (GHP/181/20GD) under the Innovation and Technology Fund of Hong Kong Special Administration Region of China and Science and Technology Planning Project of Guangdong Province (2021A0505110013). The Electron Microscope Unit at HKU is thanked for assisting SEM characterization.

Supplementary materials

Supplementary materials associated with this article can be found, in the online

version, at

References

Cai, Y., Long, X., Luo, Y.-H., Zhou, C. and Rittmann, B.E. 2021. Stable dechlorination of trichloroacetic acid (TCAA) to acetic acid catalyzed by palladium nanoparticles deposited on H_2-transfer membranes. Water Res. 192, 116841.

Castaño Osorio, S., Biesheuvel, P.M., Spruijt, E., Dykstra, J.E. and van der Wal, A. 2022. Modeling micropollutant removal by nanofiltration and reverse osmosis membranes: considerations and challenges. Water Res. 225, 119130.

Childress, A.E. and Elimelech, M. 2000. Relating nanofiltration membrane performance to membrane charge (electrokinetic) characteristics. Environ. Sci. Technol. 34(17), 3710-3716.

Costet, N., Villanueva, C.M., Jaakkola, J.J.K., Kogevinas, M., Cantor, K.P., King, W.D., Lynch, C.F., Nieuwenhuijsen, M.J. and Cordier, S. 2011. Water disinfection by-products and bladder cancer: is there a European specificity? A pooled and meta-analysis of European case–control studies. Occup. Environ. Med. 68(5), 379.

Dai, R., Wang, X., Tang, C.Y. and Wang, Z. 2020. Dually charged MOF-based thin-film nanocomposite nanofiltration membrane for enhanced removal of charged pharmaceutically active compounds. Environ. Sci. Technol. 54(12), 7619-7628.

Dai, R., Yang, Z., Qiu, Z., Long, L., Tang, C.Y. and Wang, Z. 2022. Distinct impact of substrate hydrophilicity on performance and structure of TFC NF and RO polyamide membranes. J. Membr. Sci. 662, 120966.

Dai, R., Zhou, H., Wang, T., Qiu, Z., Long, L., Lin, S., Tang, C.Y. and Wang, Z. 2023. Nanovehicle-assisted monomer shuttling enables highly permeable and selective nanofiltration membranes for water purification. Nature Water.

Ding, S., Deng, Y., Bond, T., Fang, C., Cao, Z. and Chu, W. 2019. Disinfection byproduct formation during drinking water treatment and distribution: A review of unintended effects of engineering agents and materials. Water Res. 160, 313-329.

Do, V.T., Tang, C.Y., Reinhard, M. and Leckie, J.O. 2012. Effects of hypochlorous acid exposure on the rejection of salt, polyethylene glycols, boron and arsenic(V) by nanofiltration and reverse osmosis membranes. Water Res. 46(16), 5217-5223.

Gan, Q., Peng, L.E., Guo, H., Yang, Z. and Tang, C.Y. 2022. Cosolvent-assisted interfacial polymerization toward regulating the morphology and performance of polyamide reverse osmosis membranes: Increased m-phenylenediamine solubility or enhanced interfacial vaporization? Environ. Sci. Technol. 56(14), 10308-10316.

Gan, Q., Wu, C., Long, L., Peng, L.E., Yang, Z., Guo, H. and Tang, C.Y. 2023. Does surface roughness necessarily increase the fouling propensity of polyamide reverse osmosis membranes by humic acid? Environ. Sci. Technol. 57(6), 2548-2556.

Guo, H., Dai, R., Xie, M., Peng, L.E., Yao, Z., Yang, Z., Nghiem, L.D., Snyder, S.A., Wang, Z. and Tang, C.Y. 2022a. Tweak in puzzle: tailoring membrane chemistry and structure toward targeted removal of organic micropollutants for water reuse. Environ. Sci. Technol. Lett. 9(4), 247-257.

Guo, H., Deng, Y., Yao, Z., Yang, Z., Wang, J., Lin, C., Zhang, T., Zhu, B. and Tang, C.Y. 2017. A highly selective surface coating for enhanced membrane rejection of endocrine disrupting compounds: Mechanistic insights and implications.

Water Res. 121, 197-203.
Guo, H., Li, X., Yang, W., Yao, Z., Mei, Y., Peng, L.E., Yang, Z., Shao, S. and Tang, C.Y. 2022b. Nanofiltration for drinking water treatment: a review. Front. Chem. Sci. Eng. 16(5), 681-698.
He, Q., Hu, Y., Li, X., Liu, M., Yu, S. and Gao, C. 2022. Pore size regulation of polyamide composite membrane via a sol-gel process confined within the selective layer. J. Membr. Sci. 655, 120581.
Helte, E., Säve-Söderbergh, M., Ugge, H., Fall, K., Larsson, S.C. and Åkesson, A. 2022. Chlorination by-products in drinking water and risk of bladder cancer – A population-based cohort study. Water Res. 214, 118202.
Hu, Y., Wang, F., Yang, Z. and Tang, C.Y. 2023. Modeling nanovoid-enhanced water permeance of thin film composite membranes. J. Membr. Sci., 121555.
Jiang, C., Zhang, L., Li, P., Sun, H., Hou, Y. and Niu, Q.J. 2020. Ultrathin film composite membranes fabricated by novel in situ free interfacial polymerization for desalination. ACS Appl. Mater. Interfaces 12(22), 25304-25315.
Jiang, J., Li, W., Zhang, X., Liu, J. and Zhu, X. 2018. A new approach to controlling halogenated DBPs by GAC adsorption of aromatic intermediates from chlorine disinfection: Effects of bromide and contact time. Sep. Purif. Technol. 203, 260-267.
Jiang, J., Zhang, X., Zhu, X. and Li, Y. 2017. Removal of intermediate aromatic halogenated DBPs by activated carbon adsorption: A new approach to controlling halogenated DBPs in chlorinated drinking water. Environ. Sci. Technol. 51(6), 3435-3444.
Jütte, M., Abdighahroudi, M.S., Waldminghaus, T., Lackner, S. and V. Lutze, H. 2023. Bacterial inactivation processes in water disinfection – mechanistic aspects of primary and secondary oxidants – A critical review. Water Res. 231, 119626.
Lee, Y.K., Yoo, H.-Y., Ko, K.-S., He, W., Karanfil, T. and Hur, J. 2022. Tracing microplastic (MP)-derived dissolved organic matter in the infiltration of MP-contaminated sand system and its disinfection byproducts formation. Water Res. 221, 118806.
Li, C., Sun, W., Lu, Z., Ao, X., Li, S., Wang, Z., Qi, F. and Ismailova, O. 2022. Contribution of filtration and photocatalysis to DOM removal and fouling mechanism during in-situ UV-LED photocatalytic ceramic membrane process. Water Res. 226, 119298.
Li, X.-F. and Mitch, W.A. 2018. Drinking water disinfection byproducts (DBPs) and human health effects: multidisciplinary challenges and opportunities. Environ. Sci. Technol. 52(4), 1681-1689.
Li, X., Wang, Z., Han, X., Liu, Y., Wang, C., Yan, F. and Wang, J. 2021. Regulating the interfacial polymerization process toward high-performance polyamide thin-film composite reverse osmosis and nanofiltration membranes: A review. J. Membr. Sci. 640, 119765.
Liu, M., Graham, N., Wang, W., Zhao, R., Lu, Y., Elimelech, M. and Yu, W. 2022a. Spatial assessment of tap-water safety in China. Nat. Sustain. 5(8), 689-698.
Liu, Y., Li, H., Wang, R., Hu, Q., Zhang, Y., Wang, Z., Zhou, J., Qu, G., Wang, T., Jia, H. and Zhu, L. 2022b. Underlying mechanisms of promoted formation of haloacetic acids disinfection byproducts after indometacin degradation by non-thermal discharge plasma. Water Res. 220, 118701.
Liu, Z., Zhang, Z., Peng, J., Wu, J. and Huo, Y. 2022c. Rapid removal of trace haloacetic acids from drinking water by a continuous adsorption process using graphene oxide. Environ. Technol. 43(10), 1544-1550.

Long, L., Wu, C., Yang, Z. and Tang, C.Y. 2022. Carbon nanotube interlayer enhances water permeance and antifouling performance of nanofiltration membranes: mechanisms and experimental evidence. Environ. Sci. Technol. 56(4), 2656-2664.
Long, L., Xue, Y., Zeng, Y., Yang, K. and Lin, C. 2017. Synthesis, characterization and mechanism analysis of modified crayfish shell biochar possessed ZnO nanoparticles to remove trichloroacetic acid. J. Clean. Prod. 166, 1244-1252.
Ma, X., Yang, Z., Yao, Z., Guo, H., Xu, Z. and Tang, C.Y. 2019. Tuning roughness features of thin film composite polyamide membranes for simultaneously enhanced permeability, selectivity and anti-fouling performance. J. Colloid Interface Sci. 540, 382-388.
Ma, X., Yao, Z., Yang, Z., Guo, H., Xu, Z., Tang, C.Y. and Elimelech, M. 2018. Nanofoaming of polyamide desalination membranes to tune permeability and selectivity. Environ. Sci. Technol. Lett. 5(2), 123-130.
Mazhar, M.A., Khan, N.A., Ahmed, S., Khan, A.H., Hussain, A., Rahisuddin, Changani, F., Yousefi, M., Ahmadi, S. and Vambol, V. 2020. Chlorination disinfection by-products in municipal drinking water – A review. J. Clean. Prod. 273, 123159.
Mo, Y., Tiraferri, A., Yip, N.Y., Adout, A., Huang, X. and Elimelech, M. 2012. Improved antifouling properties of polyamide nanofiltration membranes by reducing the density of surface carboxyl groups. Environ. Sci. Technol. 46(24), 13253-13261.
Peng, L.E., Gan, Q., Yang, Z., Wang, L., Sun, P.-F., Guo, H., Park, H.-D. and Tang, C.Y. 2022. Deciphering the role of amine concentration on polyamide formation toward enhanced RO performance. ACS EST Engg. 2(5), 903-912.
Peng, L.E., Yao, Z., Liu, X., Deng, B., Guo, H. and Tang, C.Y. 2019. Tailoring polyamide rejection layer with aqueous carbonate chemistry for enhanced membrane separation: mechanistic insights, chemistry-structure-property relationship, and environmental implications. Environ. Sci. Technol. 53(16), 9764-9770.
Peng, L.E., Yao, Z., Yang, Z., Guo, H. and Tang, C.Y. 2020. Dissecting the role of substrate on the morphology and separation properties of thin film composite polyamide membranes: seeing is believing. Environ. Sci. Technol. 54(11), 6978-6986.
Qiu, Z., Han, H., Wang, T., Dai, R. and Wang, Z. 2023. Nanofoaming by surfactant tunes morphology and performance of polyamide nanofiltration membrane. Desalination 552, 116457.
Samonte, P.R.V., Li, Z., Mao, J., Chaplin, B.P. and Xu, W. 2022. Pyrogenic carbon-promoted haloacetic acid decarboxylation to trihalomethanes in drinking water. Water Res. 210, 117988.
Shao, S., Zeng, F., Long, L., Zhu, X., Peng, L.E., Wang, F., Yang, Z. and Tang, C.Y. 2022. Nanofiltration membranes with crumpled polyamide films: a critical review on mechanisms, performances, and environmental applications. Environ. Sci. Technol. 56(18), 12811-12827.
Song, X., Gan, B., Qi, S., Guo, H., Tang, C.Y., Zhou, Y. and Gao, C. 2020. Intrinsic nanoscale structure of thin film composite polyamide membranes: connectivity, defects, and structure–property correlation. Environ. Sci. Technol. 54(6), 3559-3569.
Tang, C.Y., Kwon, Y.-N. and Leckie, J.O. 2009. Effect of membrane chemistry and coating layer on physiochemical properties of thin film composite polyamide RO and NF membranes: I. FTIR and XPS characterization of polyamide and

549 coating layer chemistry. Desalination 242(1), 149-167.
550 Tang, C.Y., Yang, Z., Guo, H., Wen, J.J., Nghiem, L.D. and Cornelissen, E. 2018.
551 Potable water reuse through advanced membrane technology. Environ. Sci.
552 Technol. 52(18), 10215-10223.
553 Tao, T. and Xin, K. 2014. Public health: A sustainable plan for China's drinking water.
554 Nature 511(7511), 527-528.
555 Tiraferri, A. and Elimelech, M. 2012. Direct quantification of negatively charged
556 functional groups on membrane surfaces. J. Membr. Sci. 389, 499-508.
557 Ukrainsky, B. and Ramon, G.Z. 2018. Temperature measurement of the reaction zone
558 during polyamide film formation by interfacial polymerization. J. Membr. Sci.
559 566, 329-335.
560 Villanueva, C.M., Evlampidou, I., Ibrahim, F., Donat-Vargas, C., Valentin, A., Tugulea,
561 A.-M., Echigo, S., Jovanovic, D., Lebedev, A.T., Lemus-Pérez, M., Rodriguez-
562 Susa, M., Luzati, A., de Cássia dos Santos Nery, T., Pastén, P.A., Quiñones, M.,
563 Regli, S., Weisman, R., Dong, S., Ha, M., Phattarapattamawong, S., Manasfi,
564 T., Musah, S.-I.E., Eng, A., Janák, K., Rush, S.C., Reckhow, D., Krasner, S.W.,
565 Vineis, P., Richardson, S.D. and Kogevinas, M. 2023. Global assessment of
566 chemical quality of drinking water: The case of trihalomethanes. Water Res.
567 230, 119568.
568 Wang, L., Niu, R., Chen, B., Wang, L. and Zhang, G. 2017. A comparison of
569 photodegradation kinetics, mechanisms, and products between chlorinated and
570 brominated/iodinated haloacetic acids in water. Chem. Eng. J. 330, 1326-1333.
571 Wu, C., Long, L., Yang, Z. and Tang, C.Y. 2022. Porous substrate affects fouling
572 propensity of thin-film composite nanofiltration membranes. J. Membr. Sci.
573 Lett. 2(2), 100036.
574 Yan, X., Lin, T., Wang, X., Zhang, S. and Zhou, K. 2022. Effects of pipe materials on
575 the characteristic recognition, disinfection byproduct formation, and toxicity
576 risk of pipe wall biofilms during chlorination in water supply pipelines. Water
577 Res. 210, 117980.
578 Yang, L., She, Q., Wan, M.P., Wang, R., Chang, V.W.C. and Tang, C.Y. 2017a.
579 Removal of haloacetic acids from swimming pool water by reverse osmosis and
580 nanofiltration. Water Res. 116, 116-125.
581 Yang, L., Zhou, J., She, Q., Wan, M.P., Wang, R., Chang, V.W.C. and Tang, C.Y.
582 2017b. Role of calcium ions on the removal of haloacetic acids from swimming
583 pool water by nanofiltration: mechanisms and implications. Water Res. 110,
584 332-341.
585 Yang, W., Long, L., Guo, H., Wu, C., Zhou, S., Mei, Y., Peng, L.E., Liu, W., Yang, Z.,
586 Li, W. and Tang, C.Y. 2022a. Facile synthesis of nanofiltration membrane with
587 asymmetric selectivity towards enhanced water recovery for groundwater
588 remediation. J. Membr. Sci. 663, 121038.
589 Yang, Z., Guo, H. and Tang, C.Y. 2019. The upper bound of thin-film composite (TFC)
590 polyamide membranes for desalination. J. Membr. Sci. 590, 117297.
591 Yang, Z., Long, L., Wu, C. and Tang, C.Y. 2022b. High permeance or high selectivity?
592 Optimization of system-scale nanofiltration performance constrained by the
593 upper bound. ACS EST Engg. 2(3), 377-390.
594 Yang, Z., Wu, C. and Tang, C.Y. 2023. Making waves: Why do we need ultra-
595 permeable nanofiltration membranes for water treatment? Water Res. X 19,
596 100172.
597 Yin, T., Wu, Y., Shi, P., Li, A., Xu, B., Chu, W. and Pan, Y. 2020. Anion-exchange
598 resin adsorption followed by electrolysis: A new disinfection approach to

control halogenated disinfection byproducts in drinking water. Water Res. 168, 115144.
Yuan, B., Sun, H., Zhao, S., Yang, H., Wang, P., Li, P., Sun, H. and Jason Niu, Q. 2019. Semi-aromatic polyamide nanofiltration membranes with tuned surface charge and pore size distribution designed for the efficient removal of Ca^{2+} and Mg^{2+}. Sep. Purif. Technol. 220, 162-175.
Zhang, J., Zhang, H., Liu, X., Cui, F. and Zhao, Z. 2022. Efficient reductive and oxidative decomposition of haloacetic acids by the vacuum-ultraviolet/sulfite system. Water Res. 210, 117974.
Zhang, X., Yang, W., Wang, Q., Huang, F., Gao, C. and Xue, L. 2021. Tuning the nano-porosity and nano-morphology of nano-filtration (NF) membranes: Divalent metal nitrates modulated inter-facial polymerization. J. Membr. Sci. 640, 119780.
Zhao, Y., Tong, T., Wang, X., Lin, S., Reid, E.M. and Chen, Y. 2021. Differentiating solutes with precise nanofiltration for next generation environmental separations: a review. Environ. Sci. Technol. 55(3), 1359-1376.